A full Stokes subgrid model for simulation of grounding line migration in ice sheets using Elmer/ICE(v8.3)

Gong Cheng[1], Per Lötstedt[1], and Lina von Sydow[1]

[1]Department of Information Technology, Uppsala University, P. O. Box 337, SE-75105 Uppsala, Sweden

Correspondence: Gong Cheng (cheng.gong@it.uu.se)

Abstract. The full Stokes equations are solved by a finite element method for simulation of large ice sheets and glaciers. The simulation is particularly sensitive to the discretization of the grounding line which separates the ice resting on the bedrock and the ice floating on water and is moving in time. The boundary conditions at the ice base are enforced by Nitsche's method and a subgrid treatment of the elements in the discretization close to the grounding line. Simulations with the method in two dimensions for an advancing and a retreating grounding line illustrate the performance of the method. It is implemented in the two dimensional version of the open source code Elmer/ICE.

1 Introduction

Simulation with ice sheet models is a tool to assess the future sea-level rise (SLR) due to melting of continental ice sheets and glaciers Hanna et al. (2013) and to reconstruct the ice sheets of the past DeConto and Pollard (2016); Stokes et al. (2015) for comparison with measurements and validation of the models. In the models, the predictions are particularly sensitive to the numerical treatment of the grounding line (GL) Durand and Pattyn (2015). The GL is the line where the ice sheet leaves the solid bedrock and becomes an ice shelf floating on water driven by buoyancy. It is important to know the GL position to be able to quantify the ice discharge into the sea and as an indicator if the ice sheet is advancing or retreating Konrad et al. (2018). The distance that the GL moves may be long over palaeo time scales. It is shown in Kingslake et al. (2018) that the GL has retreated several hundred km on West Antarctica during the last 11,500 years and then advanced again after the isostatic rebound of the bed. The sensitivity, long time intervals, and long distances require a careful treatment of the GL neighborhood by the numerical method to discretize the model equations.

The most accurate ice model is based on the full Stokes (FS) equations. A simplification of the FS equations by integrating in the depth of the ice is the shallow shelf (or shelfy stream) approximation (SSA) MacAyeal (1989). The computational advantage with SSA is that the dimension of the problem is reduced by one. It is often used for simulation of the interaction between a grounded ice sheet and a marine ice shelf. Several other simplifications exist with the same advantages as the SSA but with slightly different solutions. Another simplification is the shallow ice approximation (SIA) suitable for ice sheets where vertical shear stresses determine the ice flow Weis et al. (1999).

When the ice rests on the ground and is affected by frictional forces on the bed, the ice flow is dominated by vertical shear stresses. Longitudinal stresses are dominant when the ice is floating on water. The GL is in the transition zone with a gradual

change of the stress field. A SSA model for a two dimensional (2D) ice is analyzed in Schoof (2007) where there is a switch in the friction coefficient at the GL from being positive in the grounded ice to zero in the floating ice. The stability of steady state GL solutions depends on the geometry of the slope, see Schoof (2007). It is stable in a downward slope and unstable in an upward slope. In the zone between the grounded ice and the floating ice, it is necessary to use the FS equations Docquier

30   et al. (2011); Schoof (2011); Schoof and Hindmarsh (2010); Wilchinsky and Chugunov (2000) unless the ice is moving rapidly on the ground with low basal friction and the SSA equations are accurate both upstream and downstream of the GL. The solution to the linearized FS equations close to the GL is investigated using perturbation theory in Schoof (2011). The effect of perturbations in the topography and the friction coefficient on the surface velocity and height is studied in Cheng and Lötstedt (2019). The sensitivity to the perturbations increases close to the GL because the velocity of the ice increases and the thickness

35   decreases there.

   The evolution of the GL in simulations is sensitive to the ice model, the basal friction model, and numerical parameters. In a major effort MISMIP Pattyn et al. (2013, 2012), different ice models and implementations solve the same ice flow problems and the predicted GL steady state and transient GL motion are compared. The results depend on the model equations and the mesh resolution Pattyn et al. (2013). The prediction of the GL and the SLR is different for different ice equations such as FS

40   and SSA also in Pattyn and Durand (2013). Including equations with vertical shear stress at the GL such as the FS equations seems to be crucial. The friction laws at the ice base depend on the effective pressure, the basal velocity, and distance to the GL in different combinations in Brondex et al. (2017); Gagliardini et al. (2015); Gladstone et al. (2017); Leguy et al. (2014). The GL position and the SLR vary considerably depending on the choice of friction model. Given the friction model, the results are sensitive to its model parameters too Gong et al. (2017).

45   Parameters in the numerical methods also influence the GL migration. It is observed in Durand et al. (2009b) that the mesh resolution along the ice bed has to be fine to obtain reliable solutions with FS in GL simulations. The GL is then located in a node of the fixed mesh. A mesh size below 1 km is necessary in Larour et al. (2019) to resolve the features at the GL. The SIA and SSA equations model the ice close to the GL in Docquier et al. (2011). The transient response of the GL is compared with the FS equations and adaptive meshes in 2D and the SSA equations in Drouet et al. (2013). The flotation

50   condition determines where the GL is in Docquier et al. (2011); Drouet et al. (2013). It is based on Archimedes' principle for an ice column immersed in water. Another adaptive mesh method is developed for the SSA equations in 1D in Gladstone et al. (2010a). The accuracy of the method is evaluated in simulations of the GL migration. Adaptive meshes for a finite volume discretization of an approximation of the FS equations are employed in Cornford et al. (2013) to study the GL retreat and loss of ice in West Antarctica. The FS solutions of benchmark problems in Pattyn et al. (2013) computed by FEM implementations

55   in Elmer/ICE Gagliardini et al. (2013) and FELIX-S Leng et al. (2012) are compared in Zhang et al. (2017). The differences between the codes are attributed to different treatment of a friction parameter at the GL and different assignment of grounded and floating nodes and element faces.

   A subgrid model introduces an inner structure in the discretization element or mesh volume where the GL is. Such a model for the GL is tested in Gladstone et al. (2010b) for the 1D SSA equation where the flotation condition for the ice defines the

60   position of the GL. The GL migration is determined by the 2D SSA equations discretized by the finite element method (FEM)

in Seroussi et al. (2014). Subgrid models at the GL are compared to a model without an internal structure in the element. The conclusion is that sub-element parameterization is necessary. A shallow approximation to FS with subgrid modeling on coarse meshes is compared to FS in Feldmann et al. (2014) with similar results for the GL migration. Subgrid modeling and adaptivity are compared in Cornford et al. (2016) for a vertically integrated model. The stability of the GL in solutions with
65 FS and fine meshes in 2D are compared in Durand et al. (2009a) to the theory in Schoof (2007) with good agreement. A fine mesh resolution is necessary for converged GL positions with FS in Durand et al. (2009a, b). The purpose of a subgrid model is to avoid such fine meshes.

The fine mesh resolution needed in GL simulations with the FS equations would require large computational efforts in 3D to solve the equations in long time intervals. Since the GL moves long distances in palaeo simulations, a dynamic mesh refinement
70 and coarsening of the mesh following the GL is necessary. The alternative pursued here is to introduce a subgrid modeling with FEM in the mesh elements where the GL is located and keep the mesh size coarser. The subgrid model is restricted to one element in a 2D ice and is therefore computationally inexpensive. In an extension to 3D, the subgrid model would be applied along a 1D line of elements in 3D. The results with numerical modeling will always depend on the mesh resolution but can be more or less sensitive to the mesh spacing and time steps. Our subgrid modeling is aiming at improving the accuracy in GL
75 simulations for a static mesh size.

We solve the FS equations in 2D with the Galerkin method implemented in Elmer/ICE Gagliardini et al. (2013). The boundary conditions are imposed by Nitsche's method in the weak formulation of the equations Nitsche (1971); Reusken et al. (2017); Urquiza et al. (2014). The linear Stokes equations are solved in Chouly et al. (2017a) with Nitsche's treatment of the boundary conditions. They solve the equations for the displacement but here we solve for the velocity using similar numerical
80 techniques to weakly impose the Dirichlet boundary conditions. A subgrid discretization is proposed and tested for the element where the GL is located. The position of the GL within the element is determined by theory developed for the linearized FS in Schoof (2011).

The paper is organized as follows. Section 2 is devoted to the presentation of the mathematical model of the ice sheet dynamics. In Sect. 3 the numerical discretization is presented while the subgrid modeling around the GL is found in Sect. 4.
85 We present the numerical results in Sect. 5. The extension to 3D is discussed in Sect. 6 and finally some conclusions are drawn in Sect. 7.

2 Ice model

2.1 The full Stokes (FS) equations

We use the FS equations in 2D with coordinates $\mathbf{x} = (x, z)^T$ for modeling of the flow of an ice sheet Hutter (1983). These
90 nonlinear partial differential equations (PDEs) in the interior of the ice Ω are given by

$$\begin{cases} \nabla \cdot \mathbf{u} = 0, \\ -\nabla \cdot \sigma = \rho \mathbf{g}, \end{cases} \tag{1}$$

where the stress tensor is $\sigma = 2\eta(\mathbf{u})\tau(\mathbf{u}) - p\mathbb{I}$. The symmetric strain rate tensor is defined by

$$\tau(\mathbf{u}) = \frac{1}{2}(\nabla\mathbf{u} + \nabla\mathbf{u}^T) = \begin{pmatrix} \tau_{11} & \tau_{12} \\ \tau_{12} & \tau_{22} \end{pmatrix}, \tag{2}$$

$\mathbb{I}$ is the identity matrix, and the viscosity is defined by Glen's flow law

$$95 \quad \eta(\mathbf{u}) = \frac{1}{2}\left(\mathcal{A}(T')\right)^{-\frac{1}{n}} \tau_e^{\frac{1-n}{n}}, \qquad \tau_e = \sqrt{\frac{1}{2}\mathrm{tr}(\tau(\mathbf{u})\tau(\mathbf{u}))}. \tag{3}$$

Here $\mathbf{u} = (u, w)^T$ is the vector of velocities, ρ is the density of the ice, p denotes the pressure, and the gravitational acceleration in the z-direction is denoted by $\mathbf{g}$. The rate factor $\mathcal{A}(T')$ describes how the viscosity depends on the pressure melting point corrected temperature T'. For isothermal flow assumed here, the rate factor $\mathcal{A}$ is constant. Finally, n is usually taken to be 3.

100 ## 2.2 Boundary conditions
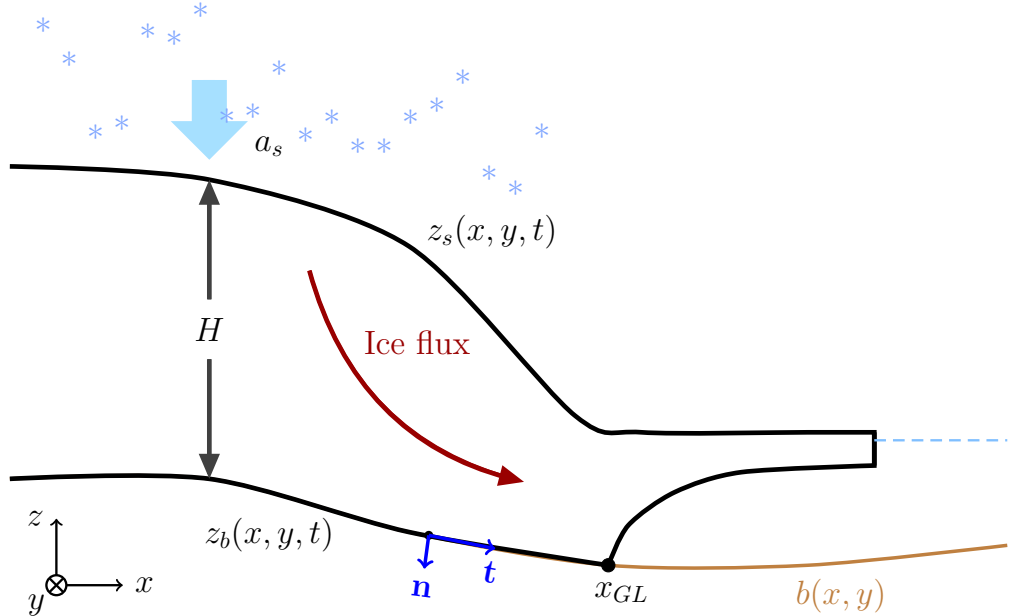
Figure 1. A two dimensional schematic view of a marine ice sheet.

At the boundary Γ of the ice we define the normal outgoing vector $\mathbf{n}$ and tangential vector $\mathbf{t}$, see Figure 1. In a 2D case considered here, y is constant in the figure. The upper boundary is denoted by Γ_s and the lower boundary is Γ_b. At Γ_s and Γ_{bf}, the floating part of Γ_b, we have that

$$\sigma\mathbf{n} = \mathbf{f}_s. \tag{4}$$

105   The ice is stress-free at Γ_s, $\mathbf{f}_s = 0$, and $\mathbf{f}_s = -p_w \mathbf{n}$ at the ice/ocean interface Γ_{bf} where p_w is the water pressure. Let

$$\sigma_{\mathbf{nt}} = \mathbf{t} \cdot \sigma \mathbf{n}, \ \sigma_{\mathbf{nn}} = \mathbf{n} \cdot \sigma \mathbf{n}, \ u_{\mathbf{t}} = \mathbf{t} \cdot \mathbf{u}.$$

Then for the slip boundary Γ_{bg}, the part of Γ_b where the ice is grounded, we have a friction law for the sliding ice

$$\sigma_{\mathbf{nt}} + \beta(\mathbf{u}, \mathbf{x})u_{\mathbf{t}} = 0, \quad u_{\mathbf{n}} = \mathbf{n} \cdot \mathbf{u} = 0, \quad -\sigma_{\mathbf{nn}} \geq p_w. \tag{5}$$

The type of friction law is determined by the friction coefficient β. There is a balance between $\sigma_{\mathbf{nn}}$ and p_w at Γ_{bf} and the

110   contact is friction-free, $\beta = 0$,

$$\sigma_{\mathbf{nt}} = 0, \qquad -\sigma_{\mathbf{nn}} = p_w. \tag{6}$$

The GL is located where the boundary condition switches from $\beta > 0$ and $u_{\mathbf{n}} = 0$ on Γ_{bg} to $\beta = 0$ and a free $u_{\mathbf{n}}$ on Γ_{bf}. In 2D, the GL is the point (x_{GL}, z_{GL}) between Γ_{bg} and Γ_{bf}.

     With the ocean surface at $z = 0$, $p_w = -\rho_w g z_b$ where ρ_w is the density of sea water, z_b is the z-coordinate of Γ_b, and g is

115   the gravitation constant.

2.3   The free surface equations

The boundaries Γ_s and Γ_b are time-dependent and move according to two free surface equations. The boundary Γ_{bg} follows the fixed bedrock with coordinates $(x, b(x))$.

     The z-coordinate of the free surface position $z_s(x, t)$ at Γ_s (see Fig. 1) is the solution of an advection equation

120    $$\frac{\partial z_s}{\partial t} + u_s \frac{\partial z_s}{\partial x} - w_s = a_s, \tag{7}$$

where a_s denotes the net surface accumulation/ablation of ice and $\mathbf{u}_s = (u_s, w_s)^T$ the velocity at the free surface in contact with the atmosphere. Similarly, the z-coordinate for the lower surface z_b of the floating ice at Γ_{bf} satisfies

$$\frac{\partial z_b}{\partial t} + u_b \frac{\partial z_b}{\partial x} - w_b = a_b, \tag{8}$$

where a_b is the net accumulation/ablation at the lower surface and $\mathbf{u}_b = (u_b, w_b)^T$ the velocity of the ice at Γ_{bf}. On Γ_{bg},

125    $z_b = b(x)$.

     The thickness of the ice is denoted by $H = z_s - z_b$ and depends on (x, t).

2.4   The solution close to the grounding line

The 2D solution of the FS equations in Eq. (1) with a constant viscosity, $n = 1$ in Eq. (3), is expanded in small parameters in Schoof (2011). The solutions in different regions around the GL are connected by matched asymptotics. Upstream of the GL at

130   the bedrock, $x < x_{GL}$, the leading terms in the expansion satisfy a simple equation in scaled variables close to the GL. Across

the GL, u, the flux of ice uH, and the depth integrated normal or longitudinal stress τ_{11} in Eq. (2) are continuous. By adding higher order terms, it is shown that the upper surface slope is continuous and Archimedes' flotation condition

$$H\rho = -z_b\rho_w \tag{9}$$

is not satisfied immediately downstream of the GL. A rapid variation in the vertical velocity w in a short interval at the GL
135   causes oscillations in the upper surface as observed also in FS simulations in Durand et al. (2009a).

In (Schoof, 2011, Ch. 4.3), the solution to the FS in 2D is expanded in two parameters ν and ϵ. The aspect ratio of the ice ν is the quotient between a typical scale of the height of the ice $\mathcal{H}$ and a length scale $\mathcal{L}$, $\nu = \mathcal{H}/\mathcal{L}$, and ϵ is ν times the quotient between the longitudinal and the shear stresses τ_{11} and τ_{12} in Eq. (2). If $\nu^{5/2} \ll \epsilon \ll 1$ then in a boundary layer close to the GL and $x < x_{GL}$ the leading terms in the solution in scaled variables satisfy

140   $$\tau_{22} - p = \sigma_{22} = \rho g(z - z_s). \tag{10}$$

On floating ice $\tau_{22} - p + p_w = 0$ and the flotation criterion Eq. (9) is fulfilled, and on the bedrock $\tau_{22} - p + p_w < 0$, see Eq. (4) and (6).

Introduce the notation

$$\chi(x,z) = \tau_{22} - p + p_w = \rho g(z - z_s(x)) - \rho_w g z_b(x), \tag{11}$$

145   and approximate z_s and z_b linearly in x in the vicinity of x_{GL} and let H_{bw} be the thickness of the ice below the water surface. Then

$$\chi(x,z_b) = -g(\rho H - \rho_w H_{bw}) \tag{12}$$

is linear in x. If $x < x_{GL}$ then $\chi < 0$ in the neighborhood of x_{GL} on Γ_{bg} and if $x > x_{GL}$ then $\chi = 0$ and Eq. (9) holds true on Γ_{bf}. In numerical experiments with the linear FS ($n = 1$) in Nowicki and Wingham (2008), $\chi(x,z_b)$ in the original variables
150   varies linearly in x for $x < x_{GL}$. In Sect. 4, $\chi(x,z_b)$ is used to estimate the GL position.

3   Discretization by FEM

In this section we state the weak form of Eq. (1) and introduce the spatial FEM discretization used for Eq. (1) and give the time-discretization of Eq. (7) and (8).

3.1   The weak form of the FS equations

155   We start by defining the mixed weak form of the FS equations. Introduce $k = 1 + 1/n$, $k^* = 1 + n$ and the spaces

$$\boldsymbol{V}_k = \{\mathbf{v} : \mathbf{v} \in (W^{1,k}(\Omega))^2\}, \quad Q_{k^*} = \{q : q \in L^{k^*}(\Omega)\}, \tag{13}$$

see, e.g. Chen et al. (2013); Martin and Monnier (2014). The weak solution $(\mathbf{u}, p)$ of Eq. (1) is obtained as follows. Find $(\mathbf{u}, p) \in \boldsymbol{V}_k \times Q_{k^*}$ such that for all $(\mathbf{v}, q) \in \boldsymbol{V}_k \times Q_{k^*}$ the equation

$$A((\mathbf{u}, p), (\mathbf{v}, q)) + B_\Gamma(\mathbf{u}, p, \mathbf{v}) + B_\mathcal{N}(\mathbf{u}, \mathbf{v}, q) = F(\mathbf{v}), \tag{14}$$

160 is satisfied, where

$$A((\mathbf{u}, p), (\mathbf{v}, q)) = \int_\Omega 2\eta(\mathbf{u})\tau(\mathbf{u}) : \tau(\mathbf{v}) \ \mathrm{d}\mathbf{x} - b(\mathbf{u}, q) - b(\mathbf{v}, p),$$

$$b(\mathbf{u}, q) = \int_\Omega q\nabla \cdot \mathbf{u} \ \mathrm{d}\mathbf{x},$$

$$B_\Gamma(\mathbf{u}, p, \mathbf{v}) = \int_{\Gamma_{bg}} (-\sigma_{\mathbf{nn}}(\mathbf{u}, p)\mathbf{n} \cdot \mathbf{v} + \beta\mathbf{u} \cdot \mathbf{v}) \ \mathrm{d}s,$$

$$B_\mathcal{N}(\mathbf{u}, \mathbf{v}, q) = -\int_{\Gamma_{bg}} \sigma_{\mathbf{nn}}(\mathbf{v}, q)\mathbf{n} \cdot \mathbf{u} \ \mathrm{d}s + \gamma_0 \int_{\Gamma_{bg}} \frac{1}{h}(\mathbf{n} \cdot \mathbf{u})(\mathbf{n} \cdot \mathbf{v}) \ \mathrm{d}s,$$

$$F(\mathbf{v}) = \int_\Omega \rho\mathbf{g} \cdot \mathbf{v} \ \mathrm{d}\mathbf{x} - \int_{\Gamma_{bf}} p_w\mathbf{n} \cdot \mathbf{v} \ \mathrm{d}s.$$

The last term in $B_\mathcal{N}$ is added in the weak form in Nitsche's method Nitsche (1971) to impose the Dirichlet condition $u_\mathbf{n} = 0$ weakly on Γ_{bg}. It can be considered as a penalty term. The size of the positive parameter γ_0 depends on the application and h is a measure of the mesh size on Γ_b. The first term in $B_\mathcal{N}$ symmetrizes the boundary term $B_\Gamma + B_\mathcal{N}$ on Γ_{bg} and vanishes when
165 $u_\mathbf{n} = 0$.

3.2   The discretized FS equations

We employ linear Lagrange elements with Galerkin Least Square (GLS) stabilization Franca and Frey (1992); Helanow and Ahlkrona (2018) to avoid spurious oscillations in the pressure using the standard setting in Elmer/ICE Gagliardini et al. (2013) approximating solutions in the spaces $\boldsymbol{V}_k$ and M_{k^*} in Eq. (13).

170   The mesh is constructed from a footprint mesh on the bottom surface and then extruded with the same number of layers in the vertical direction according to the thickness of the ice. To simplify the implementation in 2D, the footprint mesh on the bottom surface consists of $N + 1$ nodes x_i, $i = 0, \ldots, N$, with a constant mesh size Δx.

In general, the GL is somewhere in the interior of an element $\mathcal{E}_i = [x_i, x_{i+1}]$ and it crosses the element boundaries as it moves forward in the advance phase and backward in the retreat phase of the ice. The advantage with Nitsche's way of formulating
175 the boundary conditions is that if $x_{GL} \in \mathcal{E}_i$ then the boundary integral over $\mathcal{E}_i$ can be split into two parts in Eq. (14) such that

$[x_i, x_{GL}] \in \Gamma_{bg}$ and $[x_{GL}, x_{i+1}] \in \Gamma_{bf}$ as follows

$$
\begin{aligned}
&\int_{\mathcal{E}_i} B_\Gamma + B_\mathcal{N} \ \mathrm{d}s \\
&= \int_{[x_i, x_{GL}]} -(\sigma_{\mathbf{nn}}(\mathbf{u}, p)\mathbf{n} \cdot \mathbf{v} + \sigma_{\mathbf{nn}}(\mathbf{v}, q)\mathbf{n} \cdot \mathbf{u}) \\
&\quad + \beta\mathbf{u} \cdot \mathbf{v} + \frac{\gamma_0}{h}(\mathbf{n} \cdot \mathbf{u})(\mathbf{n} \cdot \mathbf{v}) \ \mathrm{d}s + \int_{[x_{GL}, x_{i+1}]} p_w \mathbf{n} \cdot \mathbf{v} \ \mathrm{d}s.
\end{aligned}
\tag{15}
$$

There is a change of boundary conditions in the middle of the element $\mathcal{E}_i$ where the GL is located. With a strong formulation of $u_{\mathbf{n}} = 0$ the basis functions in $\boldsymbol{V}_s$ share this property and the condition changes from the grounded node x_i where the basis function satisfies $u_{\mathbf{n}} = 0$ and the floating node at x_{i+1} with a free $u_{\mathbf{n}}$ without taking the position of the GL inside $\mathcal{E}_i$ into account.

The resulting system of non-linear equations form a nonlinear complementarity problem Christensen et al. (1998). The distance d between the base of the ice and the bedrock at time t and at x is $d = z_b(x,t) - b(x) \geq 0$. If $d > 0$ on Γ_{bf} then the ice is not in contact with the bedrock and $\sigma_{\mathbf{nn}} + p_w = 0$ and if $\sigma_{\mathbf{nn}} + p_w < 0$ on Γ_{bg} then the ice and the bedrock are in contact and $d = 0$. Hence, the complementarity relation in the vertical direction is

$$
\begin{aligned}
&z_b(x,t) - b(x) \geq 0, \ \sigma_{\mathbf{nn}} + p_w \leq 0, \\
&(z_b(x,t) - b(x))(\sigma_{\mathbf{nn}} + p_w) = 0 \text{ on } \Gamma_b.
\end{aligned}
\tag{16}
$$

The contact friction law is such that $\beta > 0$ when $x < x_{GL}$ and $\beta = 0$ when $x > x_{GL}$. The complementarity relation along the slope at x is then the non-negativity of d and

$$
\beta \geq 0, \ \beta(x,t)(z_b(x,t) - b(x)) = 0 \text{ on } \Gamma_b.
\tag{17}
$$

In particular, these relations are valid at the nodes $x = x_j, \ j = 0, 1, \ldots, N$.

The complementarity condition also holds for $u_{\mathbf{n}}$ and $\sigma_{\mathbf{nn}}$ such that

$$
\begin{aligned}
&\sigma_{\mathbf{nn}} + p_w \leq 0, \\
&u_{\mathbf{n}}(\sigma_{\mathbf{nn}} + p_w) = 0 \text{ on } \Gamma_b,
\end{aligned}
\tag{18}
$$

without any sign constraint on $u_{\mathbf{n}}$ except for the retreat phase when the ice leaves the ground and $u_{\mathbf{n}} < 0$.

Similar implementations for contact problems using Nitsche's method are found in Chouly et al. (2017a, b), where the unknowns in the PDEs are the displacement fields instead of the velocity in Eq. (1). Analysis in Chouly et al. (2017a) suggests that Nitsche's method for the contact problem can provide a stable numerical solution with an optimal convergence rate.

The nonlinear equations for the nodal values of $\mathbf{u}$ and p are solved by Newton iterations. The system of linear equations in every Newton iteration is solved iteratively by using the Generalised Conjugate Residual (GCR) method in Elmer/ICE. The condition on d_j in a node x_j is used for a so called grounded mask, which is computed at each timestep and not changed during the nonlinear iterations.

3.3 Discretization of the advection equations

The advection equations for the moving ice boundary in Eq. (7) and (8) are discretized in time by a finite difference method and in space by FEM with linear Lagrange elements for z_s and z_b. A stabilization term is added, making the spatial discretization behave like an upwind scheme in the direction of the velocity as implemented in Elmer/ICE.

205 The advection equations Eq. (7) and Eq. (8) are integrated in time by a semi-implicit method of first order accuracy. Let $c = s$ or b. Then the solution is advanced from time t^n to $t^{n+1} = t^n + \Delta t$ with the timestep Δt by

$$z_c^{n+1} = z_c^n + \Delta t \left(a_c^n - u_c^n \frac{\partial z_c^{n+1}}{\partial x} + w_c^n \right). \tag{19}$$

The spatial derivative of z_c is approximated by FEM. A system of linear equations is solved at t^{n+1} for z_c^{n+1}. This time discretization and its properties are discussed in Cheng et al. (2017).

210 A stability problem in z_b is encountered in the boundary condition at Γ_{bf} in Durand et al. (2009a). It is solved by expressing z_b in p_w at Γ_{bf} with a damping term in Durand et al. (2009a). An alternative interpretation of the idea in Durand et al. (2009a) and an explanation follow below.

The relation between $u_\mathbf{n}$ and $u_\mathbf{t}$ at Γ_{bf} and $\mathbf{u}_b = \mathbf{u}(x, z_b(x))$ is

$$\mathbf{u}_b = \begin{pmatrix} u_b \\ w_b \end{pmatrix} = \begin{pmatrix} z_{bx} \\ -1 \end{pmatrix} \frac{u_\mathbf{n}}{\sqrt{1 + z_{bx}^2}} + \begin{pmatrix} 1 \\ z_{bx} \end{pmatrix} \frac{u_\mathbf{t}}{\sqrt{1 + z_{bx}^2}}, \tag{20}$$

215 where z_{bx} denotes $\partial z_b / \partial x$. Insert u_b and w_b from Eq. (20) into Eq. (8) to obtain

$$\frac{\partial z_b}{\partial t} = a_b - u_\mathbf{n} \sqrt{1 + z_{bx}^2}, \tag{21}$$

Instead of discretizing Eq. (21) explicitly at t^n with $u_\mathbf{n}^{n-1}$ to determine p_w^n, the base coordinate is updated implicitly

$$z_b^n = z_b^{n-1} + \Delta t \left(a_b^n - u_\mathbf{n}^n \sqrt{1 + z_{bx}^2} \right) \tag{22}$$

in the solution of Eq. (14).

220 Assume that z_{bx} is small. The timestep restriction in Eq. (22) is estimated by considering a 2D slab of the floating ice of width Δx and thickness H. Newton's law of motion yields

$$M \dot{u}_\mathbf{n} = Mg - \Delta x p_w,$$

where $M = \Delta x (z_s - z_b) \rho$ is the mass of the slab. Divide by M, integrate in time for $u_\mathbf{n}(t^m)$, let $m = n$ or $n-1$, and approximate the integral by the trapezoidal rule for the quadrature to obtain

$$u_\mathbf{n}(t^m) = \int_0^{t^m} g + \frac{g\rho_w}{\rho} \frac{z_b}{z_s - z_b} \, \mathrm{d}s$$

$$\approx g t^m + \frac{g\rho_w}{\rho} \sum_{i=0}^{m} \alpha_i \frac{z_b^i}{z_s^i - z_b^i} \Delta t,$$

225

$$\alpha_i = 0.5, i = 0, m, \quad \alpha_i = 1, i = 1, \ldots, m-1.$$

Then insert $u_{\mathbf{n}}^m$ into Eq. (22). All terms in $u_{\mathbf{n}}^m$ from timesteps $i < m$ are collected in the sum $\Delta t F^{m-1}$. Then Eq. (22) can be written

230
$$z_b^n = z_b^{n-1} - \Delta t^2 \frac{g\rho_w}{2\rho} \frac{z_b^m}{z_s^m - z_b^m} + \Delta t \left(a_b^n - gt^m - \Delta t F^{m-1} \right). \qquad (23)$$

For small changes in z_b in Eq. (23), the explicit method with $m = n-1$ is stable when Δt is so small that

$$\left| 1 - \Delta t^2 \frac{g\rho_w}{2H\rho} \right| \leq 1. \qquad (24)$$

When $H = 100$ m on the ice shelf, $\Delta t < 6.1$ s which is far smaller than the stable steps for Eq. (19). Choosing the implicit scheme with $m = n$, the bound on Δt is

235
$$1/\left| 1 + \Delta t^2 \frac{g\rho_w}{2H\rho} \right| \leq 1, \qquad (25)$$

i.e. there is no bound on positive Δt for stability but accuracy will restrict Δt.

Much longer stable timesteps are possible at the surface and the base of the ice with a semi-implicit method Eq. (19) and a fully implicit method Eq. (22) compared to an explicit method. For example, the timestep for the problem in Eq. (19) with 1 km mesh size can be up to a couple of months. Therefore, we use the scheme in Eq. (19) for Eq. (7) and (8) and the scheme
240 in Eq. (22) for Eq. (21) and p_w as in Durand et al. (2009a). The difference between the approximations of z_b in Eq. (19) and (22) is of $\mathcal{O}(\Delta t^2)$.

4   Subgrid modeling around grounding line

The basic idea of the subgrid method for the FS equations in this paper follows the GL parameterization for SSA in Seroussi et al. (2014) and the analysis for FS in Schoof (2011). The GL is located at the position where the ice is on the ground and
245 the flotation criterion is perfectly satisfied such that $\sigma_{\mathbf{nn}} = -p_w$. In the Stokes equations, the hydrostatic assumption may not be valid, so the exact GL position can not be determined by simply checking the total thickness of the ice H against the depth below sea level $H_{bw} = -z_b$. Instead, the flotation criterion is computed by comparing the water pressure with the normal stress component orthogonal to the boundary as indicated by the first order analysis in Sect. 2.4. The indicator is here defined by $\chi(x) = \sigma_{\mathbf{nn}} + p_w$ which vanishes on the floating ice and is approximately $\tau_{22} - p + p_w$ and negative on the ground since the
250 slope of the bedrock is small.

Typically, at the lower surface of the floating ice where $z_b(x,t) > b(x)$, as the blue line in Fig. 2, the boundary conditions are given by Eq. (6), and where the ice is in contact with the bedrock, as the red line in Fig. 2, the boundary conditions are given by Eq. (5). However, there is another case as shown in Fig. 3 when the net force at x_i is pointing inward, namely $\sigma_{\mathbf{nn}}(x_i) + p_w(x_i) > 0$. Then, the floating boundary condition Eq. (6) should be imposed up until the node x_{i-1}. This can happen
255 at some point due to the low spatial and temporal resolutions, but the node x_i will move upward as long as $\mathbf{u} \cdot \mathbf{n} < 0$, or the net

force switches signs and the condition transforms into the case in Fig. 2 when $\sigma_{\mathbf{nn}}(x_i) + p_w(x_i) < 0$. Denote the situation in Fig. 2 by case i, and the one in Fig. 3 by case ii. We call the node 'grounded' when it is in contact with the bedrock with net force from the ice pointing outward ($\sigma_{\mathbf{nn}} + p_w < 0$), and 'floating' when the net force is pointing inward ($\sigma_{\mathbf{nn}} + p_w \geq 0$). The element which contains both grounded and floating nodes is called the GL element and the grounded node in it is called the

260   last grounded node and the floating one is called the first floating node.

In coarse meshes, the true position of the GL is generally not in one of the nodes, but usually between the last grounded and the first floating nodes. Instead of refining the mesh around GL, which would lead to very small time steps for stability reasons, we will here introduce a subgrid model for the GL element.

We let $\chi(x) = \sigma_{\mathbf{nn}}(x) + p_w(x)$ and assume that it is linear as in Eq. (11) to determine the position of the GL, x_{GL}, in the GL

265   element. In case ii, the GL is located between x_{i-1} and x_i even though the whole element $[x_{i-1}, x_i]$ is geometrically grounded. The equation $\chi(x_{GL}) = 0$ is solved by linear interpolation between $\chi(x_{i-1}) < 0$ and $\chi(x_i) > 0$ yielding a unique solution satisfying $x_{i-1} < x_{GL} < x_i$, depicted as the red dot in the lower panel of Fig. 3.

There is a more complicated situation in case i, where $\chi(x_i) < 0$ but $\chi(x_{i+1}) = 0$ due to the floating boundary condition. A correction of χ is made by using $\tilde{\chi}(x) = \sigma_{\mathbf{nn}}(x) + p_b(x)$ where $p_b(x) = -\rho_w g b(x)$ is the water pressure on the bedrock. For

270    $x > x_i$, we have $b(x) < z_b(x)$ and $p_b(x) > p_w(x)$. Therefore, $\tilde{\chi}(x_{i+1}) > \chi(x_{i+1}) = 0$ and $\tilde{\chi}(x_i) = \chi(x_i) < 0$. Then, a linear interpolation between $\tilde{\chi}(x_i)$ and $\tilde{\chi}(x_{i+1})$ guarantees a unique solution of $\tilde{\chi}(x_{GL}) = 0$ in the GL element $[x_i, x_{i+1}]$, see Fig. 2. In case ii, p_b can also be used since $p_b(x) = p_w(x)$ as long as the element is on the bedrock.

Conceptually, the linear interpolation of the function $\tilde{\chi}(x)$ can be considered separately by looking at the two linear functions $\sigma_{\mathbf{nn}}(x)$ and $p_b(x)$. As the GL always rests on the bedrock, $p_b(x_{GL}) = p_w(x_{GL})$ is actually an exact representation of the water

275   pressure imposed on the ice at GL, although geometrically $z_b(x_{GL})$ may not coincide with $b(x_{GL})$, especially on coarse meshes. This also leads to the fact that the interpolated normal stress $\sigma_{\mathbf{nn}}(x_{GL}, z_b(x_{GL}))$ is a first order approximation of the normal stress at the exact GL position $(x_{GL}, b(x_{GL}))$.

This correction is not necessary when the GL is advancing since the implicit treatment of the bottom surface is equivalent to additional water pressure at the stress boundary as discussed in Sect. 3.3.

280   After the GL position is determined, the domains Γ_{bg} and Γ_{bf} are separated at x_{GL} as in Eq. (15) and the integrals are calculated with a high-order integration scheme as in Seroussi et al. (2014) to achieve a better resolution within the element shown in Figures 2 and 3. For a smoother transition of β at GL, the slip coefficient is multiplied by 1/2 at the whole GL element before integrating using the high order scheme.

The penalty term from Nitsche's method restricts the motion of the element in the normal direction. It should only be

285   imposed on the element which is fully on the ground. On the contrary, in case i, the GL element $[x_i, x_{i+1}]$ is not in contact with the bedrock as in Fig. 2, so only the floating boundary condition should be used on the element $[x_i, x_{i+1}]$. Additionally, the implicit representation of the bottom surface in Eq. (22) also implies that the case ii with retreating GL should be merged to case i since the surface is leaving the bedrock and the normal velocity should not be forced to zero. To summarize, Nitsche's penalty term should be imposed on all the fully grounded elements and partially on the GL element in the advance phase.
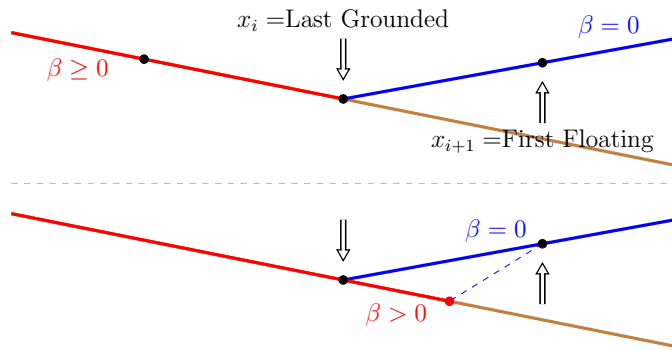
Figure 2. Schematic figure of Grounding Line in case i. Upper panel: the last grounded and first floating nodes as defined in Elmer/ICE. Lower panel: linear interpolation to compute a more accurate position of the Grounding Line.
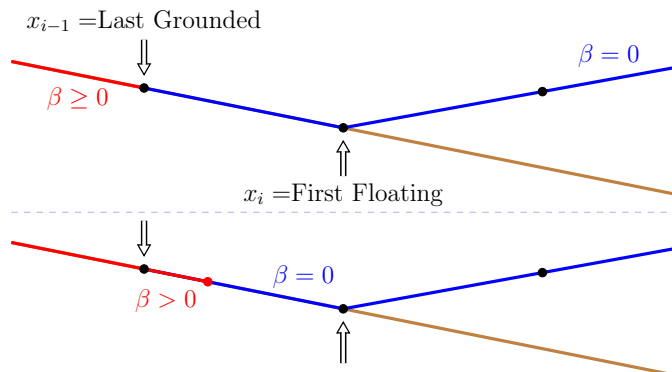
Figure 3. Schematic figure of Grounding Line in case ii. Upper panel: the last grounded and first floating nodes as defined in Elmer/ICE. Lower panel: linear interpolation to compute a more accurate position of the Grounding Line.

290   Equations (1), (7), and (8) form a system of coupled nonlinear equations. They are solved in the same manner as in Elmer/ICE v.8.3. The x_{GL} position is determined dynamically within every nonlinear iteration when solving the FS equations and the high order integrations are based on the current x_{GL}. The nonlinear FS is solved with fixed-point iterations to 10^{-5} relative error with a limit of maximal 25 nonlinear iterations and the grounded condition is set if the distance between of the bottom surface and the bedrock is smaller than 10^{-3} m.

5   Results

The numerical experiments follow the MISMIP benchmark Pattyn et al. (2012) and comparison is made with the results in Gagliardini et al. (2016). Using the experiment MISMIP 3a, the setups are exactly the same as in the advancing and retreating simulations in Gagliardini et al. (2016). The experiments are run with spatial resolutions of $\Delta x = 4$ km, 2 km and 1 km with

20 vertical extruded layers. The timestep is $\Delta t = 0.125$ year for all the three resolutions to eliminate time discretization errors

300   when comparing different spatial resolutions.

The dependence on γ_0 for the retreating ice is shown in Fig. 4 with γ_0 between 10^4 and 10^9. The estimated GL positions do not vary with different choices of γ_0 from 10^5 to 10^8 which suggests a suitable range of γ_0. If γ_0 is too small ($\gamma_0 \ll 10^4$), oscillations appear in the estimated GL positions. If γ_0 is too large ($\gamma_0 \gg 10^8$), then more nonlinear iterations are needed for each time step. The same dependency of γ_0 is observed for the advance experiments and for different mesh resolutions as well.

305   For the remaining experiments, we fix $\gamma_0 = 10^6$.
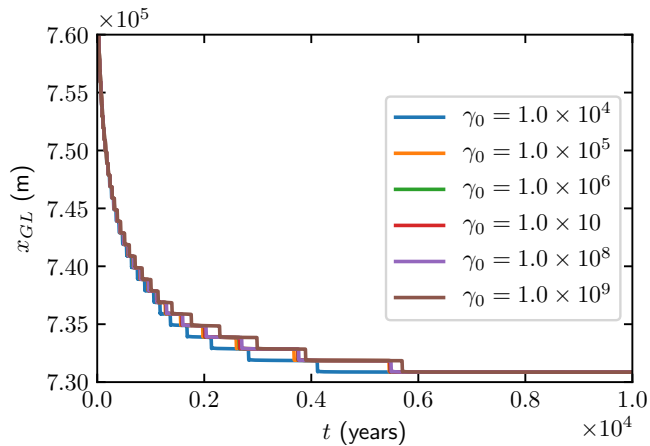
Figure 4. The MISMIP 3a retreat experiment with $\Delta x = 1000$ m for different choices of γ_0 in the time interval $[0, 10000]$ years.

The GL position during 10000 years in the advance and retreat phases are displayed in Fig. 5 for different mesh sizes. The range of the results from Gagliardini et al. (2016) with mesh resolutions $\Delta x = 25$ and 50 m are shown as background shaded regions with colors purple and pink. We achieve similar GL migration results both for the advance and retreat experiments with at least 20 times larger mesh sizes.

310   We observed oscillations at the top surface near the GL in all the experiments as expected from Durand et al. (2009a); Schoof (2011). A zoom-in plot of the surface elevation with $\Delta x = 1$ km at $t = 10000$ years is shown to the left in Fig. 6, where the red dashed line indicates the estimated GL position. Obviously, the estimated GL position does not coincide with any nodes even at the steady state.

The ratio between the thickness below sea level H_{bw} and the ice thickness H is shown in Fig. 6. The horizontal, purple,

315   dash-dotted line indicates the ratio of ρ/ρ_w and the estimated GL is located at the red, dashed line. This result confirms that the hydrostatic assumption $H\rho = H_{bw}\rho_w$ is not valid in the FS equations for $x > x_{GL}$ close to the GL and at the GL position, cf. Durand et al. (2009a); Schoof (2011). For $x < x_{GL}$ we have that $H_{bw}/H < \rho/\rho_w$ since H_{bw} decreases and H increases. The conclusion from numerical experiments in Van Dongen et al. (2018) is that the hydrostatic assumption and the SSA equations approximate the FS equations well for the floating ice beginning at a short distance away from the GL.
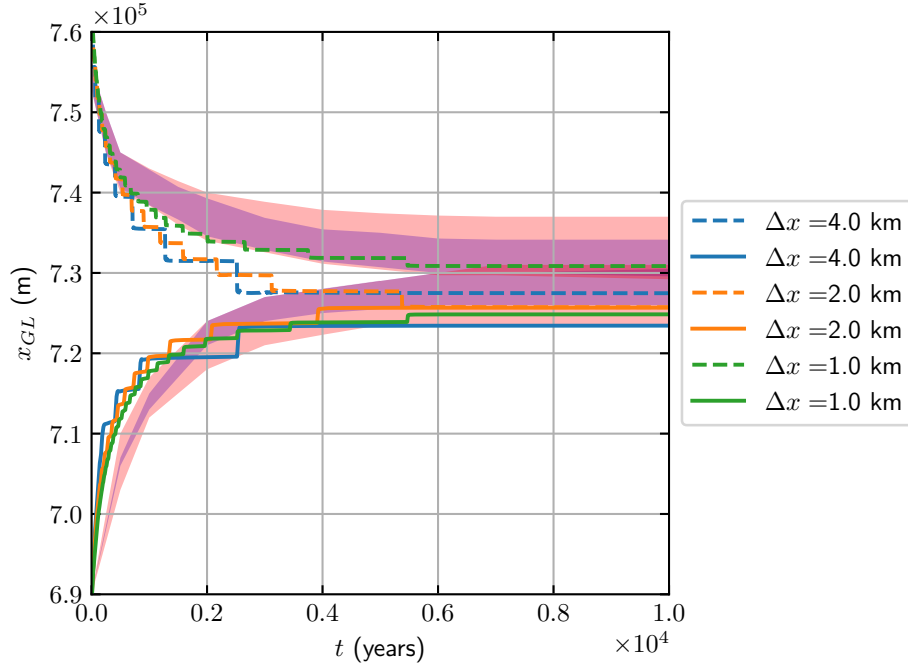
Figure 5. The MISMIP 3a experiments for the GL position when $t \in [0, 10000]$ with $\Delta x = 4000, 2000$ and 1000 m for the advance (solid) and retreat (dashed) phases. The shaded regions indicate the range of the results in Gagliardini et al. (2016) with $\Delta x = 50$ m in red and $\Delta x = 25$ m in blue.

320   The top and bottom surface velocity solutions from the retreat experiment are shown in Fig. 7 with $\Delta x = 1$ km after 10000 years. The horizontal velocities on the two surfaces are similar with negligibly small differences on the floating ice. The vertical velocities w on the top (orange line) and bottom surface (blue line) at the GL are almost discontinuous as analyzed in Schoof (2011). With the subgrid method, the rapid variation is resolved by the 1 km mesh size.

6   Discussion

325   Seroussi et al Seroussi et al. (2014) describe four different subgrid models for the friction in SSA and evaluate them in a FEM discretization on a triangulated, planar domain. The flotation criterion is applied at the nodes of the triangles. Depending on how many of the nodes that are floating, the amount of friction in the triangle is determined. Also, a higher order polynomial integration over the triangles in FEM allows an inner structure in the triangular element.

Our method can be extended to a triangular mesh covering Γ_b in the following way. The condition on χ in Eq. (11) is applied
330   on the edges of each triangle $\mathcal{T}$ in the mesh. If $\chi < 0$ in all three nodes then $\mathcal{T}$ is grounded. If $\chi \geq 0$ in all nodes then $\mathcal{T}$ is floating. The GL passes inside $\mathcal{T}$ if χ has a different sign in one of the nodes. Then the GL crosses the two edges where $\chi < 0$
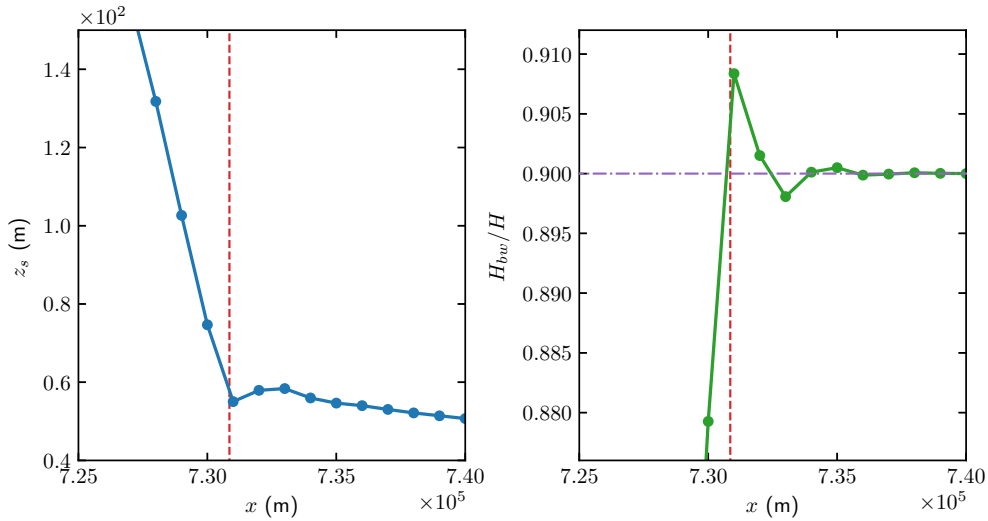
Figure 6. Details of the solutions for the retreat experiment with $\Delta x = 1$ km after 10000 years. The solid dots represent the nodes of the elements and the vertical, red, dashed lines indicate the GL position. *Left panel*: The oscillations at top surface near GL. *Right panel*: The flotation criterion is evaluated by H_{bw}/H. The ratio between ρ/ρ_w is drawn in a horizontal, purple, dash-dotted line.

in one node and $\chi \geq 0$ in the other node. In this way, a continuous reconstruction of a piecewise linear GL is possible on Γ_b. The FEM approximation is modified in the same manner as in Sect. 4 with Nitsche's method.

335   An alternative to subgrid modeling is to introduce dynamic adaptation of the mesh on Γ_b with a refinement at the GL as in e.g. Cornford et al. (2013); Drouet et al. (2013); Gladstone et al. (2010a). In general, a fine mesh is needed along the GL and in an area surrounding it. Since the GL moves long distances at least in simulations of palaeo-ice sheets, the adaptation should be dynamic, permit refinement and coarsening of the mesh, and be based on some estimate of the model inaccuracy. Furthermore, shorter timesteps are necessary for stability when the mesh size is smaller in a mesh adaptive method. Introducing a time dependent mesh adaptivity into an existing code requires a substantial coding effort and will increase the computational
340   work considerably. Subgrid modeling is easier to implement and the increase in computing time is small.

7   Conclusions

Subgrid models at the GL have been developed and tested in the SSA model for 2D flow in Gladstone et al. (2010b) and for 3D flow in Seroussi et al. (2014), for the friction in the vertically integrated model BISICLES Cornford et al. (2013) for 3D flow in Cornford et al. (2016), and for the PISM model mixing SIA with SSA in 3D in Feldmann et al. (2014). Here we propose a
345   subgrid model in 2D for the FS equations implemented in Elmer/ICE that can be extended to 3D. The mesh is static and the moving GL position within one element is determined by linear interpolation with an auxiliary function $\tilde{\chi}$ based on the theory in Schoof (2011). Only in that element, the FEM discretization is modified.
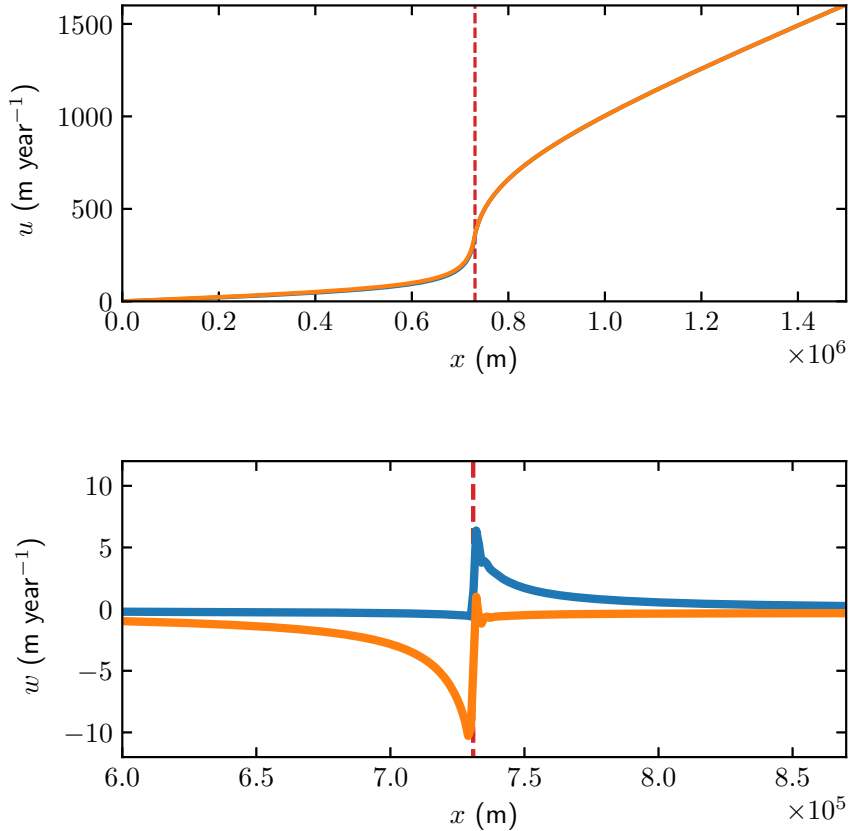
Figure 7. The velocities u (upper panel) and w (lower panel) on the top (orange) and bottom (blue) surface of the ice in the retreat experiment with $\Delta x = 1$ km after 10000 years. The red, dashed line indicates the GL position. The vertical velocity w is zoomed-in close to the GL.

The method is applied to the simulation of an ice sheet in 2D with an advancing GL and one with a retreating GL. The data for the tests are the same as in one of the MISMIP examples Pattyn et al. (2012) and in Gagliardini et al. (2016). Comparable results to Gagliardini et al. (2016) are obtained with subgrid modeling with more than 20 times larger mesh sizes. A larger mesh size also allows a longer timestep for the time integration. Without further knowledge of the basal conditions and detailed models at the GL, solving $\tilde{\chi}(x) = 0$ provides a good approximation of the GL position.

Code availability. The FS sub-grid model is implemented based on Elmer/ICE Version: 8. 3(Rev: f6bfdc9) with the scripts at http://doi.org/10.5281/zenodo.3401478 and http://doi.org/10.5281/zenodo.3401475.

355 *Author contributions.* GC developed the model code and performed the simulations. GC and PL contributed to the theory of the paper. GC, PL and LvS contributed to the development of the method and the writing of the paper

Competing interests. The authors declare that they have no conflict of interest.

Acknowledgements. This work has been supported by Nina Kirchner's Formas grant 2017-00665 and the Swedish e-Science initiative eSSENCE. We are grateful to Thomas Zwinger for advise and help in the implementation of the subgrid model in Elmer/ICE. The compu-
360 tations were performed on resources provided by the Swedish National Infrastructure for Computing (SNIC) at the PDC Center for High Performance Computing, KTH Royal Institute of Technology.

References

Brondex, J., Gagliardini, O., Gillet-Chaulet, F., and Durand, G.: Sensitivity of grounding line dynamics to the choice of the friction law, J. Glaciology, 63, 854–866, 2017.

Chen, Q., Gunzburger, M., and Perego, M.: Well-posedness results for a nonlinear Stokes problem arising in glaciology, SIAM Journal on Mathematical Analysis, 45, 2710–2733, 2013.

Cheng, G. and Lötstedt, P.: Parameter sensitivity analysis of dynamic ice sheet models-Numerical computations, The Cryosphere Discussions, 2019, 1–28, 2019.

Cheng, G., Lötstedt, P., and von Sydow, L.: Accurate and stable time stepping in ice sheet modeling, Journal of Computational Physics, 329, 29–47, 2017.

Chouly, F., Fabre, M., Hild, P., Mlika, R., Pousin, J., and Renard, Y.: An overview of recent results on Nitsche's method for contact problems, in: Geometrically unfitted finite element methods and applications, pp. 93–141, Springer, 2017a.

Chouly, F., Hild, P., Lleras, V., and Renard, Y.: Nitsche-based finite element method for contact with Coulomb friction, in: European Conference on Numerical Mathematics and Advanced Applications, pp. 839–847, Springer, 2017b.

Christensen, P. W., Klarbring, A., Pang, J. S., and Strömberg, N.: Formulation and comparison of algorithms for frictional contact problems, Int. J. Num. Meth. Eng., 42, 145–173, 1998.

Cornford, S., Martin, D., Lee, V., Payne, A., and Ng, E.: Adaptive mesh refinement versus subgrid friction interpolation in simulations of Antarctic ice dynamics, Ann. Glaciol., 57, 1–9, 2016.

Cornford, S. L., Martin, D. F., Graves, D. T., Ranken, D. F., Brocq, A. M. L., Gladstone, R. M., Payne, A. J., Ng, E. G., and Lipscomb, W. H.: Adaptive mesh, finite volume modeling of marine ice sheets, J. Comput. Phys., 232, 529–549, 2013.

DeConto, R. M. and Pollard, D.: Contribution of Antarctica to past and future sea-level rise, Nature, 531, 591–597, 2016.

Docquier, D., Perichon, L., and Pattyn, F.: Representing grounding line dynamics in numerical ice sheet models: Recent advances and outlook, Surv. Geophys., 32, 417–435, 2011.

Van Dongen, E. C., Kirchner, N., Van Gijzen, M. B., Van De Wal, R. S., Zwinger, T., Cheng, G., Lötstedt, P., and Von Sydow, L.: Dynamically coupling full Stokes and shallow shelf approximation for marine ice sheet flow using Elmer/ICE (v8. 3), Geoscientific Model Development, 11, 4563–4576, 2018.

Drouet, A. S., Docquier, D., Durand, G., Hindmarsh, R., Pattyn, F., Gagliardini, O., and Zwinger, T.: Grounding line transient response in marine ice sheet models, Cryosphere, 7, 395–406, 2013.

Durand, G. and Pattyn, F.: Reducing uncertainties in projections of Antarctic ice mass loss, Cryosphere, 9, 2043–2055, 2015.

Durand, G., Gagliardini, O., de Fleurian, B., Zwinger, T., and Le Meur, E.: Marine ice sheet dynamics: Hysteresis and neutral equilibrium, J. Geophys. Res.: Earth Surf., 114, F03 009, 2009a.

Durand, G., Gagliardini, O., Zwinger, T., Le Meur, E., and Hindmarsh, R. C. A.: Full Stokes modeling of marine ice sheets: influence of the grid size, Ann. Glaciol., 50, 109–114, 2009b.

Feldmann, J., Albrecht, T., Khroulev, C., Pattyn, F., and Levermann, A.: Resolution-dependent performance of grounding line motion in a shallow model compared with a full-Stokes model according to the MISMIP3d intercomparison, J. Glaciol., 60, 353–360, 2014.

Franca, L. P. and Frey, S. L.: Stabilized finite element methods: II. The incompressible Navier-Stokes equations, Computer Methods in Applied Mechanics and Engineering, 99, 209–233, 1992.

Gagliardini, O., Zwinger, T., Gillet-Chaulet, F., Durand, G., Favier, L., de Fleurian, B., Greve, R., Malinen, M., Martín, C., Råback, P., Ruokolainen, J., Sacchettini, M., Schäfer, M., Seddik, H., and Thies, J.: Capabilities and performance of Elmer/Ice, a new generation

400   ice-sheet model, Geosci. Model Dev., 6, 1299–1318, 2013.

Gagliardini, O., Brondex, J., Gillet-Chaulet, F., Tavard, L., Peyraud, V., and Durand, G.: On the substantial influence of the treatment of friction at the grounding line, Cryosphere, 9, 3475–3501, 2015.

Gagliardini, O., Brondex, J., Gillet-Chaulet, F., Tavard, L., Peyaud, V., and Durand, G.: Impact of mesh resolution for MISMIP and MIS-MIP3d experiments using Elmer/ICE, The Cryosphere, 10, 307–312, 2016.

405   Gladstone, R. M., Lee, V., Vieli, A., and Payne, A. J.: Grounding line migration in an adaptive mesh ice sheet model, J. Geophys. Res., 115, F04 014, 2010a.

Gladstone, R. M., Payne, A. J., and Cornford, S. L.: Parameterising the grounding line in flow-line ice sheet models, Cryosphere, 4, 605–619, 2010b.

Gladstone, R. M., Warner, R. C., Galton-Fenzi, B. K., Gagliardini, O., Zwinger, T., and Greve, R.: Marine ice sheet model performance

410   depends on basal sliding physics and sub-shelf melting, Cryosphere, 11, 319–329, 2017.

Gong, Y., Zwinger, T., Cornford, S., Gladstone, R., Schäfer, M., and Moore, J. C.: Importance of basal boundary conditions in transient simulations: case study of a surging marine-terminating glacier on Austfonna, Svalbard, J. Glaciol., 63, 106–117, 2017.

Hanna, E., Navarro, F. J., Pattyn, F., Domingues, C. M., Fettweis, X., Ivins, E. R., Nicholls, R. J., Ritz, C., Smith, B., Tulaczyk, S., White-house, P. L., and Zwally, H. J.: Ice-sheet mass balance and climate change, Nature, 498, 51–59, 2013.

415   Helanow, C. and Ahlkrona, J.: Stabilized equal low-order finite elements in ice sheet modeling–accuracy and robustness, Computational Geosciences, 22, 951–974, 2018.

Hutter, K.: Theoretical Glaciology, D. Reidel Publishing Company, Terra Scientific Publishing Company, Dordrecht, 1983.

Kingslake, J., Scherer, R. P., Albrecht, T., Coenen, J., Powell, R. D., Reese, R., Stansell, N. D., Tulaczyk, S., Wearing, M. G., and Whitehouse, P. L.: Extensive retreat and re-advance of the West Antarctic ice sheet during the Holocene, Nature, 558, 430–434, 2018.

420   Konrad, H., Shepherd, A., Gilbert, L., Hogg, A. E., McMillan, M., Muir, A., and Slater, T.: Net retreat of Antarctic glacier grounding line, Nat. Geosci., 11, 258–262, 2018.

Larour, E., Seroussi, H., Adhikari, S., Ivins, E., Caron, L., Morlighem, M., and Schlegel, N.: Slowdown in Antarctic mass loss from solid Earth and sea-level feedbacks, Science, 364, eaav7908, 2019.

Leguy, G. R., Asay-Davis, X. S., and Lipscomb, W. H.: Parameterization of basal friction near grounding lines in a one-dimensional ice sheet

425   model, Cryosphere, 8, 1239–1259, 2014.

Leng, W., Ju, L., Gunzburger, M., Price, S., and Ringler, T.: A parallel high-order accurate finite element nonlinear Stokes ice sheet model and benchmark experiments, J. Geophys. Res.: Earth Surf., 117, 2156–2202, 2012.

MacAyeal, D. R.: Large-scale ice flow over a viscous basal sediment: Theory and application to Ice Stream B, Antarctica., J. Geophys. Res., 94, 4071–4078, 1989.

430   Martin, N. and Monnier, J.: Four-field finite element solver and sensitivities for quasi-Newtonian flows, SIAM Journal on Scientific Computing, 36, S132–S165, 2014.

Nitsche, J.: Über ein Variationsprinzip zur Lösung von Dirichlet-Problemen bei Verwendung von Teilräumen, die keinen Randbedingungen unterworfen sind, Abh. Math. Semin., University of Hamburg, Germany, 36, 9–15, 1971.

Nowicki, S. M. J. and Wingham, D. J.: Conditions for a steady ice sheet–ice shelf junction, Earth Plan. Sci. Lett., 265, 246–255, 2008.

435   Pattyn, F. and Durand, G.: Why marine ice sheet model predictions may diverge in estimating future sea level rise, Geophys. Res. Lett., 40, 4316–4320, 2013.

Pattyn, F., Schoof, C., Perichon, L., Hindmarsh, R. C. A., Bueler, E., de Fleurian, B., Durand, G., Gagliardini, O., Gladstone, R., Goldberg, D., Gudmundsson, G. H., Huybrechts, P., Lee, V., Nick, F. M., Payne, A. J., Pollard, D., Rybak, O., Saito, F., and Vieli, A.: Results of the Marine Ice Sheet Model Intercomparison Project, MISMIP, Cryosphere, 6, 573–588, 2012.

440   Pattyn, F., Perichon, L., Durand, G., Favier, L., Gagliardini, O., Hindmarsh, R. C. A., Zwinger, T., Albrecht, T., Cornford, S., Docquier, D., Fürst, J. J., Goldberg, D., Gudmundsson, G. H., Humbert, A., Hütten, M., Jouvet, G., Kleiner, T., Larour, E., Martin, D., Morlighem, M., Payne, A. J., Pollard, D., Rückamp, M., Rybak, O., Seroussi, H., Thoma, M., and Wilkens, N.: Grounding-line migration in plan-view marine ice-sheet models: results of the ice2sea MISMIP3d intercomparison, J. Glaciol., 59, 410–422, 2013.

Reusken, A., Xu, X., and Zhang, L.: Finite element methods for a class of continuum models for immiscible flows with moving contact lines,

445   Int. J. Numer. Meth. Fluids, 84, 268–291, 2017.

Schoof, C.: Ice sheet grounding line dynamics: Steady states, stability and hysteresis, J. Geophys. Res.: Earth Surf., 112, F03S28, 2007.

Schoof, C.: Marine ice sheet dynamics. Part 2. A Stokes flow contact problem, J. Fluid Mech., 679, 122–155, 2011.

Schoof, C. and Hindmarsh, R.: Thin-Film Flows with Wall Slip: An Asymptotic Analysis of Higher Order Glacier Flow Models, Quart. J. Mech. Appl. Math., 63, 73–114, 2010.

450   Seroussi, H., Morlighem, M., Larour, E., Rignot, E., and Khazendar, A.: Hydrostatic grounding line parameterization in ice sheet models, Cryosphere, 8, 2075–2087, 2014.

Stokes, C. R., Tarasov, L., Blomdin, R., Cronin, T. M., Fisher, T. G., Gyllencreutz, R., Hättestrand, C., Heyman, J., Hindmarsh, R. C. A., Hughes, A. L. C., Jakobsson, M., Kirchner, N., Livingstone, S. J., Margold, M., Murton, J. B., Noormets, R., Peltier, W. R., Peteet, D. M., Piper, D. J. W., Preusser, F., Renssen, H., Roberts, D. H., Roche, D. M., Saint-Ange, F., and Stroeven, A. P.: On the reconstruction of

455   palaeo-ice sheets: Recent advances and future challenges, Quat. Sci. Rev., 125, 15–49, 2015.

Urquiza, J. M., Garon, A., and Farinas, M.-I.: Weak imposition of the slip boundary condition on curved boundaries for Stokes flow, J. Comput. Phys., 256, 748–767, 2014.

Weis, M., Greve, R., and Hutter, K.: Theory of shallow ice shelves, Continuum Mech. Thermodyn., 11, 15–50, 1999.

Wilchinsky, A. V. and Chugunov, V. A.: Ice-stream–ice-shelf transition: theoretical analysis of two-dimensional flow, Ann. Glaciology, 30,

460   153–162, 2000.

Zhang, T., Price, S., Ju, L., Lei, W., Brondex, J., Durand, G., and Gagliardini, O.: A comparison of two Stokes ice sheet models applied to the Marine Ice Sheet Model Intercomparison Project for plan view models, Cryosphere, 11, 179–190, 2017.